Applied Surface Science 602 (2022) 154274

Contents lists available at ScienceDirect

Applied Surface Science

journal homepage: www.elsevier.com/locate/apsusc

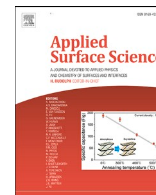

Full Length Article

Phase change in GeTe/Sb_2Te_3 superlattices: Formation of the vacancy-ordered metastable cubic structure via Ge migration

Chang Woo Lee [a,1], Jin-Su Oh [b,1], Sun-Ho Park [c,1], Hyeon Wook Lim [a], Da Sol Kim [a], Kyu-Jin Cho [b], Cheol-Woong Yang [b], Young-Kyun Kwon [c,d,*], Mann-Ho Cho [a,e,*]

[a] Department of Physics, Yonsei University, Seoul 120-749, Republic of Korea
[b] School of Advanced Materials Science and Engineering, Sungkyunkwan University, Suwon 16419, Republic of Korea
[c] Department of Physics, Kyung Hee University, Seoul 02447, Republic of Korea
[d] Department of Information Display and Research Institute for Basic Sciences, Kyung Hee University, Seoul 02447, Republic of Korea
[e] Department of System Semiconductor Engineering, Yonsei University, Seoul 03722, Republic of Korea

A R T I C L E I N F O

Keywords:
Superlattice
GeTe/Sb_2Te_3 thin film
Epitaxial thin films
Metavalent bonding
Metal-to-insulator transition
Interfacial phase-change materials
Reversible bond-switching
Phase-change mechanism
Vacancy layer
DFT calculation

A B S T R A C T

Interfacial phase-change memory (iPCM), comprising alternating layers of two chalcogenide-based phase-change materials—Sb_2Te_3 (ST) and GeTe (GT)—has demonstrated outstanding performance in resistive memories. However, its comprehensive understanding is controversial. Herein, the phase-change characteristic of iPCM is identified using atomic scale imaging, X-ray diffraction, and chemical analysis with first-principles density functional theory (DFT) calculations. By inducing laser pulsing, the ST/GT superlattice structure in the low-resistance state tends to reversibly convert into the modified metastable face-centered cubic (fcc) GeSbTe structure in the high-resistance state. This transition is driven by Ge atom rearrangement to pre-existing vacancy layers and ordered vacancy-layer formation. DFT atomistic modeling shows that the resistance difference of 10^2 orders between low- and high-resistance states is a direct consequence of the intercalation of Ge atoms into the vacancy layer. These results provide insights into iPCM phase-change mechanisms and phase-change random access memory design with low energy and high speed.

1. Introduction

Phase-change random access memory (PCRAM) is a promising candidate for next-generation nonvolatile memory and in-memory computing applications because of its high speed, high endurance, and excellent scalability compared with other nonvolatile memories. [1–7] The typical phase change between the amorphous and crystalline phases of GeTe-Sb_2Te_3 alloys existing along the pseudo-binary line can be controlled by the Joule heating process. A promising phase change material, namely, the superlattice (SL) structure of $\{GeTe/Sb_2Te_3\}_n$, was proposed. The interfacial phase-change memory (iPCM) using the proposed structure demonstrated ultra-high set speed, low power consumption, and stable cyclability by driving atomic switching. The operation method exploiting crystal-to-crystal phase changes could effectively reduce the operation energy for the phase change. To understand the uniqueness of iPCM, detailed information on the specific microstructure of the set and reset states are required for systematically improving via materials optimization. [8,9].

Several iPCM switching mechanisms were proposed, while ensuring the structural stability of iPCM, based on four phases, namely Kooi, Petrov, inverted-Petrov, and Ferro. [10–12] Tominaga et al. [13] proposed an electrical field-assisted flipping of Ge layers, resulting in a phase-transition between the Ferro-GeTe (Te-Sb-Te-Sb-Te/Ge-Te-Ge-Te/Te-Sb-Te-Sb-Te) and inverted-Petrov (Te-Sb-Te-Sb-Te/Te-Ge-Ge-Te/Te-Sb-Te-Sb-Te) structures. Kolobov et al. [14] and Chen et al. [15] proposed an alternative phase transition process; the defect reconfiguration near a van der Waals (vdW) gap results in an inversion transition of the Sb-Te bilayer between the Kooi (Te-Sb-Te-Sb-Te/Te-Sb-Te-Ge-Te-Ge-Te-Sb-Te/ Te-Sb-Te-Sb-Te) and Ferro-GeTe structures. Studies have utilized these two models to determine the transition mechanism, [15,16] mainly through microstructural analysis. Recently, transmission electron microscopy (TEM) experiments and density functional theory

* Corresponding authors at: Department of Physics, Kyung Hee University, Seoul 02447, Republic of Korea (Y. Kwon). Department of Physics, Yonsei University, Seoul 120-749, Republic of Korea (M. Cho).

E-mail addresses: cwyang@skku.edu (C.-W. Yang), ykkwon@khu.ac.kr (Y.-K. Kwon), mh.cho@yonsei.ac.kr (M.-H. Cho).

[1] These authors contributed equally to this study: C. W. Lee, J.-S. Oh, and S. Park.

https://doi.org/10.1016/j.apsusc.2022.154274
Received 24 March 2022; Received in revised form 8 July 2022; Accepted 12 July 2022
Available online 16 July 2022
0169-4332/© 2022 Elsevier B.V. All rights reserved.

(DFT) calculations demonstrated that the atomic structures of the iPCM differed from those of the existing models in explaining low- (LRS) and high-resistance (HRS) states. [11,17–22] iPCM determined that Ge and Sb atoms inevitably intermixed [11,17] and that Ge atoms were predominantly located near the GeSbTe (GST) block core in the GeTe/ Sb_2Te_3 SL. [11,18,19] Additionally, randomly distributed vacancies in GST building units were transformed into ordered vacancy layers. [20] Vacancies ordering drives a cubic-to-hexagonal structural transition and metal-to-insulator transition. [23,24] These ordered vacancy layers differ from the vdW layer because the distance across the former is larger than that across the latter. Furthermore, the GST blocks comprising nine layers with a composition ratio of Ge 1: Sb 2: Te 4, thus forming seven layers ideally, which inevitably contain several vacancies. [21] These observations strongly suggest that a new phase-change model is required comprehensively.

This study investigates the iPCM switching mechanism using structural models based on experimental findings and *ab-initio* DFT calculations. First, a large-scale iPCM phase transition was performed through in-situ laser pulse-induced reversible crystalline-to-crystalline phase transformation. Phase changes through laser pulsing are advantageous for obtaining physical information), which could provide comprehensive and precise information regarding the phase change, as it can be applied to a larger area compared with electrical pulsing on a smaller sub-micron size area. Cross-sectional TEM analysis revealed that cubic-GeSbTe (c-GST) blocks could form and *de*-form during the phase transition between the HRS and LRS. The data showed that a well-aligned SL structure, with alternating ST/GT layers (Te-Sb-Te-Sb-Te/Te-Ge-Te-Ge-Te-Ge-Te/Te-Sb-Te-Sb-Te) corresponding to the LRS, could be transformed into another crystalline SL structure containing GST layers corresponding to the HRS via Ge atom rearrangement and vacancies. This transition from the stable GeTe/Sb_2Te_3 SL LRS phase to the metastable cubic phase is directly related to the significant resistance difference between the LRS and HRS, since this transition accompanies the metal-to-insulator transition induced by the ordering of the vacancies. [25–27] The chemical states and crystalline structures of two SL structures were determined by XPS using laser pulsing; the data showed the local structural changes through Ge atom migration and vacancy rearrangement. These findings regarding the distinctive structural characteristics between two crystalline phases will provide new insights into the GeTe/ Sb_2Te_3 SL switching mechanism.

2. Results and discussion

A thin film with a GeTe/Sb_2Te_3 SL structure is fabricated using molecular beam epitaxy (MBE), where the GeTe thickness is controlled from 4 nm to 1 nm and the Sb_2Te_3 thickness is fixed at 1 nm, as shown in Supplementary Fig. S1. The phase-change process was investigated using epitaxial SL films [Sb_2Te_3 (1 nm)/ GeTe (1 nm)]$_5$/ Sb_2Te_3 (10 nm) grown on *n*-type Si (1 1 1), which showed high c-axis-orientation and well-ordered crystalline films, as shown in the XRD and Raman spectroscopy in Fig. 1a and 1b, respectively. To obtain detailed information on the stacking sequences of the SL and atomic arrangement in each layer, the intensity profile of a high angle annular dark-field scanning transmission electron microscopy (HAADF-STEM) image for an as-deposited SL was investigated, as shown in Fig. 1c. According to the principle of Z-contrast dependence on atomic numbers in TEM, the intensity of Te was similar to Sb, while the intensity of Ge was significantly lower. The 7-layered GeTe block intensity profile, which was a low-intensity profile located at the center of the block, indicated that the corresponding layer was composed of Ge atoms. Conversely, the intensity profile considered as corresponding to the Ge layer at the edge of the block was higher than at the center of the block. This result suggested that the layer at the edge of the block was intermixed rather than composed only of Ge, as shown in Fig. 1d. [11,17] Additionally, the

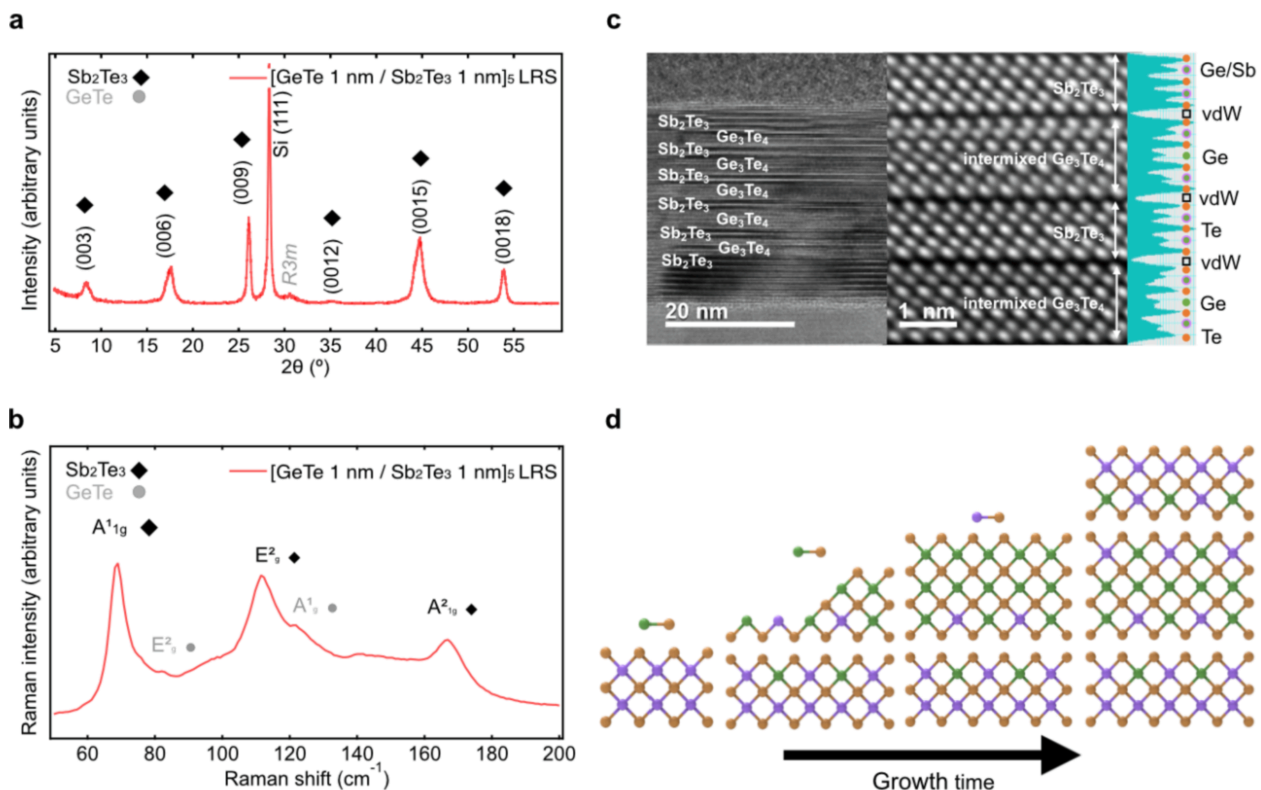

Fig. 1. [Sb_2Te_3 (1 nm)/ GeTe (1 nm)]$_5$/ Sb_2Te_3 (10 nm) SLs epitaxial thin films grown by MBE. a) XRD θ-2θ scan. b) Raman spectra of [Sb_2Te_3 (1 nm)/ GeTe (1 nm)]$_5$/ Sb_2Te_3 10 nm SL. The peaks corresponding to the Sb_2Te_3 hexagonal phase were dominant. The peaks corresponding to the GeTe rhombohedral phase[29] were slightly observed. c) HAADF image of an as-deposited SL. The GeTe block grew with the Te plane termination on the surface. d) Schematics of Ge/Sb inter-diffusion during SL growth; Ge, Sb, and Te atoms are shown in green, purple, and orange, respectively.

observed stacking sequences in the as-deposited GeTe block were entirely different from the four proposed sequences (Petrov, inverted Petrov, Kooi, and Ferro phases); i.e., the GeTe block was constituted with odd layers (7 layers) and Te-terminated surfaces as shown at the block edges, which was inconsistent with reports on the GeTe block with even layers (6 layers). This is consistent with the reported total energy of the odd layers of a GeTe block in a GeTe/Sb_2Te_3 SL structure. [28] These observations strongly indicated that previously proposed switching models for iPCM should be revised with consideration to the Te-terminated GeTe block and Ge/Sb intermixing.

To investigate the GeTe/Sb_2Te_3 SL structure switching process through the phase transition between two crystalline structures, a laser pulse-induced phase transition from the set state (LRS) to reset state (HRS) was executed. It was verified that the resistance change could be reversibly achieved through the laser pulsing and annealing processes, as shown in Fig. 2a. Resistance drift, which had been a critical problem to the reliability of conventional PCRAM operation, was scarcely observed because an amorphous phase with structural instability was not involved, as shown in Fig. 2b. During drift, resistance (R) is typically described by the power-law equation [1]:

$$R(t) = R_0\left(\frac{t}{t_0}\right)^{\nu} \tag{1}$$

where R_0 is the resistance at a reference time t_0 and ν is the power-law time exponent. [30,31] In the GeTe/Sb_2Te_3 SL, the time exponent value was estimated to be 0.04 in the set state and 0.003 in the reset state, both of which are extremely low compared with other reported values for the conventional GST alloy (~0.1). [30].

To directly observe the phase change in the GeTe/Sb_2Te_3 SL, the atomic configuration was visualized after the laser pulsing process using TEM, as shown in Fig. 2c. Although the generated structure was similar to the $Ge_2Sb_2Te_5$ hexagonal phase, composed of a nonuple atom layer, it showed inconsistencies with the hexagonal close-packed (hcp) GST structure. The XRD data supports the formation of a metastable c-GST structure in a long-range order rather than the hcp GST, as shown in Fig. 2d, because this type of GST structure in the reset state (HRS), generated after the laser pulsing process, reverted to the same structure as the LRS state after the annealing process, as shown in Supplementary Fig. S2a. We observed the reversible change at peak positions ranging from 50° to 55°. Both LRS and re-LRS both have peaks at 53.7°, whereas both HRS and re-HRS both have peaks at 52.4°. Although the XRD peaks were similar because of the structural similarity between the fcc and hcp, the GST peak in the HRS was more consistent with fcc (2 2 2) (52.4°) than hcp (0010) (53.2°) (Supplementary Fig. S2b). [32].

To comprehend detailed atomic movements in the SLs, an in-situ TEM study, which is the preferred analytical tool for elucidating atomic movements, was conducted. Structural changes were observed by comparing the atomic images in identical regions of the SL film of HRS after laser pulsing (Supplementary Fig. S3a) with the LRS during in-situ annealing (Supplementary Fig. S3b). The comparison shows that the gap in the LRS resulted from the relocation of Ge atoms in the HRS; i.e., the gap formed through the moving of the centered Ge atoms in the GST block to the two nearest neighboring cation layers. The GST blocks in HRS therefore tended to split into blocks with fewer atomic layers. A comparison of the white dashed line boxes in Supplementary Fig. S3a and Fig. S3b revealed that several bilayer defects, marked by orange ellipses, were formed through the transition, which was accompanied by a cation–anion inversion, thus lowering the number of vdW block layers. Simultaneously, new vdW gaps formed as indicated by the yellow arrow in Supplementary Fig. S3d. Thus, during a reverse phase transition from

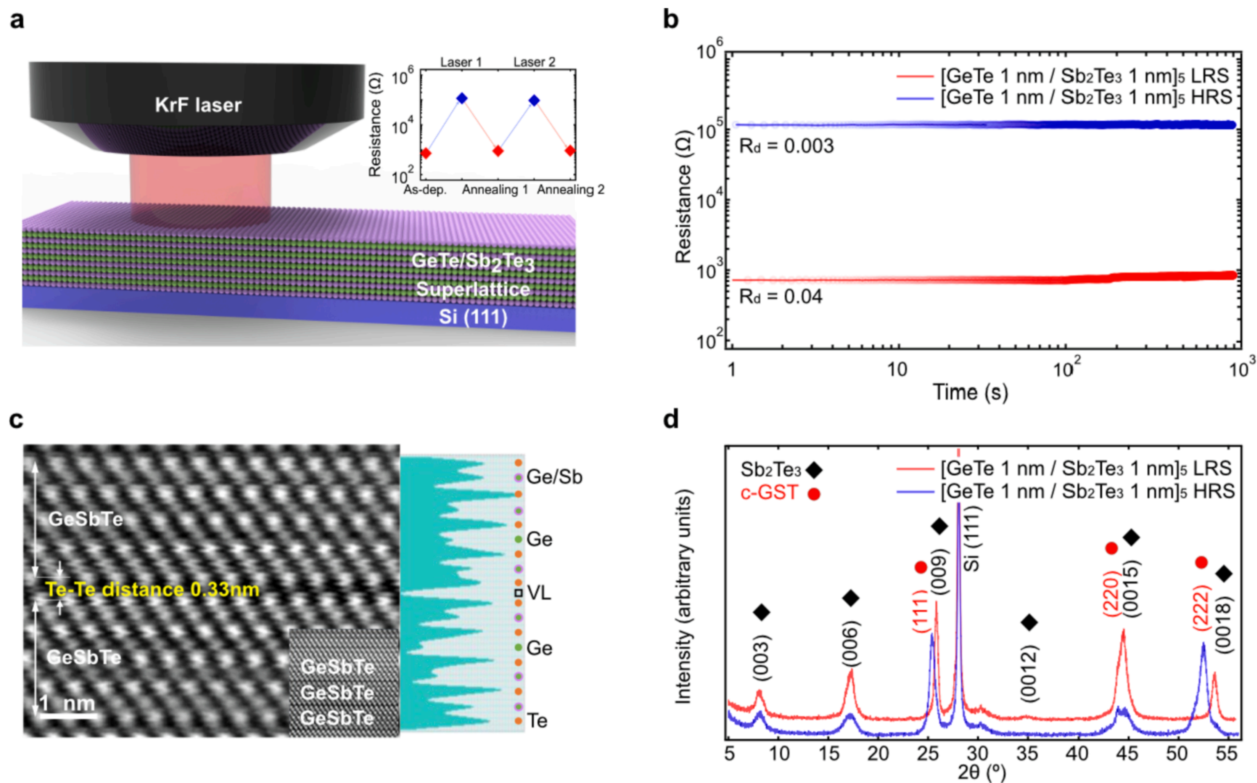

Fig. 2. Crystal structure of laser-irradiated [Sb_2Te_3 (1 nm)/ GeTe (1 nm)]$_5$/ Sb_2Te_3 10 nm SLs. a) Schematic of KrF laser pulse-inducing phase-change process. The inset shows changes in the resistances of as-deposited, laser pulse-induced, annealed, and re-laser pulse-induced samples measured along the vertical axis. b) Measured resistances as a function of time for the two SLs representing the LRS and HRS. R_d is the power-law time exponent, which indicates the degree of resistance drift. Both LRS and HRS resistances were nearly constant constants because both states maintained their crystalline phases. c) HAADF image of the laser pulse induced SLs. An ordered vacancy layer with a Te-Te distance longer than the archetypical vdW gap was formed. d) XRD θ-2θ scan in laser-pulse induced [Sb_2Te_3 (1 nm)/ GeTe (1 nm)]$_5$/ Sb_2Te_3 10 nm SLs. The formation of a face-centered c-GST structure was confirmed in the long-range order.

the LRS to HRS, the neighboring Ge atoms in the GeTe block move into the vdW gap, thus dissolving the vdW gap. After the in-situ TEM annealing process was applied to the film with the HRS, it was confirmed that the phase transition was a reversible process as the LRS phase, transformed from the HRS phase, exhibited identical structural order of the as-deposited SL, as shown in Fig. 3. Fig. 3a, 3b, and 3c depict atomic-resolution HAADF-STEM images of an as-deposited SL, laser-pulsed SL, and annealed SL, respectively. In HRS, the cation layers inside the newly formed 5-fold Te-layered GST blocks could be identified by the difference in column intensity in the middle of the blocks (see red arrow in Fig. 3b) and that near the edge of blocks (see blue arrow in Fig. 3b). The distance in the vdW gap and that between the Te layers at the edge of GeTe and Sb_2Te_3 in the LRS differed from that in the HRS. It is established that the distance between Te layers along the [0001] direction in the conventional hcp GST structure is 0.25–0.28 nm due to vdW bonding, [33] while the distance between Te layers in the metastable face-centered cubic (fcc) structure is 0.33–0.36 nm. [34] This difference suggested that the gap was not a vdW gap; the gap resulted from the vacancy layer that was ordered in a layered direction. The generation of a vacancy layer and Ge atomic migration at the edge of the GeTe block indicated that the vacancy layer of the HRS was formed through the migration of Ge atoms to the pre-existing vdW gap. Therefore, the Te-v-Te distance increased by $\geq$ 10 % to 0.33 nm because certain Ge atoms were located at the vacancy site within the vacancy layer (Fig. 2c). In addition, we confirmed that when the HRS superlattice was heat-treated at 230 °C for 10 min, it returned to the LRS Ge $2p_{3/2}$ peak again. This result confirms that the sample changed by laser experiences a reversible change and returns to its initial state through heat treatment (Fig. S4).

XPS measurements were conducted to clarify the phase-change characteristics between the set and reset states from the modulation in chemical bonding states caused by local environment changes. Noticeable chemical bond changes were observed in the XPS spectra before and after the phase change in the Ge 3d core level state. The Ge 3d spectrum binding energy data of the HRS film showed a distinctive difference compared with that of the LRS film, as shown in Supplementary Fig. S5, i.e., after the phase change induced by the laser pulsing process, the intensity of $Ge^{\text{distorted octahedral}}$ ($Ge\text{-}Te_4$) in the reset state is enhanced, while that of $Ge^{\text{octahedral}}$ ($Ge\text{-}Te_6$) in the set state decreased. Further evidence for the presence of two different chemical components in the HRS was provided by the Ge $2p_{3/2}$ level, as shown in Fig. 4a. The single chemical environment for the hexagonal phase depicts the contrast to the rock-salt structure with metavalent bonding well, wherein all Ge positions possess an identical binding energy of 1217.95 eV at Ge $2p$ level. Ge-Te chemical bonds are categorized into two: three short bonds and three long bonds. Accordingly, we observe a relatively high binding energy for a reduced length of the Ge-Te bonds and appropriately low binding energy for an increased bond length. The chemical bond for $Ge\text{-}Te_6$ is consistent with the octahedral local environment of the metastable cubic phase. Moreover, the relationship between the binding energy and bond length agrees with the proposed spinel structure ($Ge\text{-}Te_4$) with covalent bonding. [35] These results indicate that modulating the bond length changes both the bond strength and charge transfer between the neighbors. Therefore, in the LRS phase, the Ge atoms were octahedrally coordinated (metavalent bonding), as revealed by the Ge 3d and Ge $2p_{3/2}$ core levels. Conversely, in the HRS a distortion in the octahedrally coordinated (covalent bonding) Ge atoms was induced in the GST structure, as revealed by the Ge 3d and Ge $2p_{3/2}$ core levels. The binding energy of the Ge $2p_{3/2}$ core level in the HRS was inconsistent with the chemical environment produced by the recognized c-GST phase with a rock-salt structure shown in Supplementary Figs. S6a and S6b. [36–40] To understand the differences in the chemical state, we analyzed the images taken before and after the phase transition at the point HAADF-STEM marked through e-beam dosing, as shown in Supplementary Figs. S6c and S7d. Structural changes were observed by comparing the atomic images taken at identical regions. Although the number of anion layers was unchanged during annealing process in the

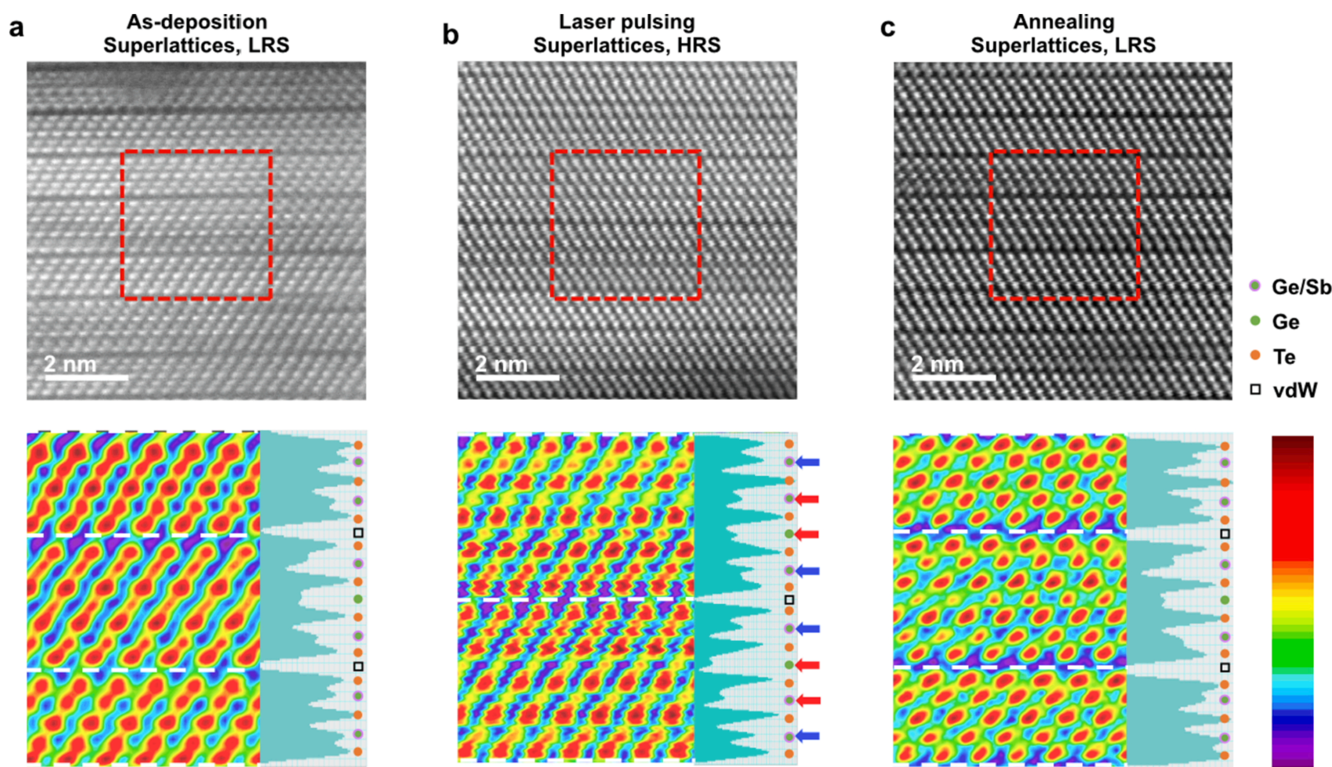

Fig. 3. HAADF-STEM image and atomic intensity profiling in the reversible phase-change process between set and reset. a) Atomic-resolution HAADF-STEM image of the as-deposited SLs acquired before in-situ laser pulsing. b) Atomic-resolution HAADF-STEM image of the HRS SLs acquired after in-situ laser pulsing. c) Atomic-resolution HAADF-STEM image of the LRS SL after in-situ TEM annealing at 200 ℃ for 30 min. Averaged intensity profiles were extracted from the orange area. The color map expresses the intensity profiling level from red to purple.

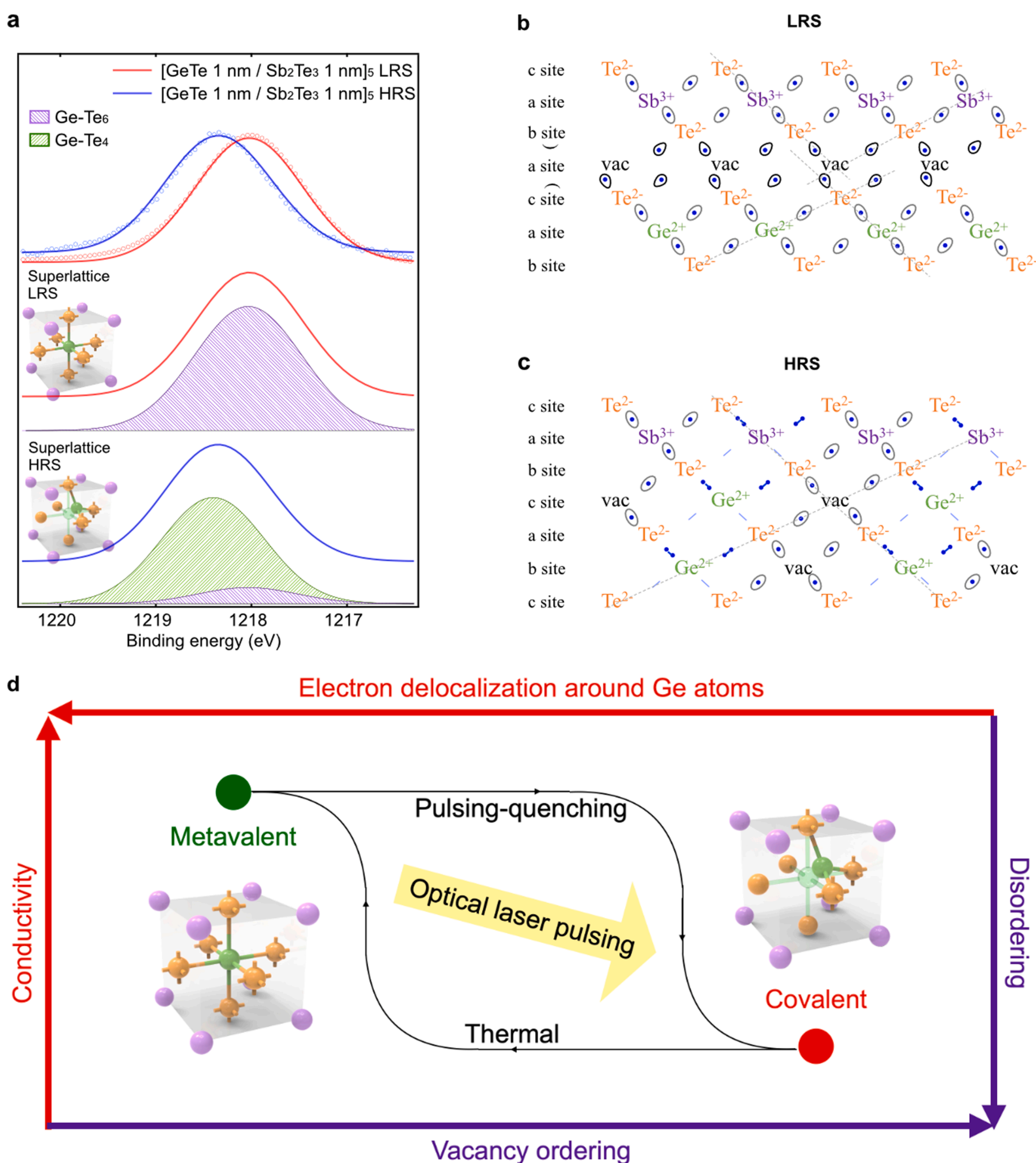

Fig. 4. Local environments of Ge in $[Sb_2Te_3$ (1 nm)/ GeTe (1 nm)$]_5$/ Sb_2Te_3 10 nm SLs in the LRS and HRS. Ge, Te, and second nearest atoms from Ge are particularly indicated using three colors, green, orange, and purple, respectively. a) Deep core-level spectra of Ge $2p_{3/2}$ measured in $[Sb_2Te_3$ (1 nm)/ GeTe (1 nm)$]_5$/ Sb_2Te_3 10 nm SLs corresponded to the LRS (red) and HRS (blue). The measured data and fitted lines were represented by circles and lines, respectively. The structural information was confirmed by the two deconvoluted peaks of the Ge $2p_{3/2}$ spectrum corresponding to the binding energies at 1218 and 1218.3 eV corresponding to the rock-salt and spinel structures, respectively. [41,42,35] Schematic diagrams depict the bonding states of the b) LRS and c) HRS. Based on the result of fitting the Ge $2p_{3/2}$ spectra in detail, the local Ge structure of the LRS was composed solely of octahedral structures. Conversely, the Ge $2p_{3/2}$ spectra in the HRS indicated that certain octahedral structures were maintained in the distorted octahedral structures. d) Schematic illustration of optical laser pulsing for iPCM phase transition. A dot in each elliptical shape represents metavalent bonding caused by the delocalized charge distribution, where each line connecting two dots denotes covalent bonding resulting from the localized charge distribution. In the LRS, Ge atoms are bonded by metavalent bonding; however, in the HRS, the Ge atoms are bonded by covalent bonding because of the formation of extrinsic vacancies that changed the local structure. Additionally, the ABC stacking changed because the hcp structure transformed into the fcc structure during the phase change.

regime depicted between the two white dash lines, the number of cation (vacancy) layers was decreased (increased) by 1. Because the number of Ge, Sb, and Te atoms were conserved, some vacancies must be contained in the cation layers in HRS. In particular, the covalent bonding ($Ge\text{-}Te_4$) is formed with $Ge\text{-}Te_6$ in HRS, as shown in Fig. 4a, which is different from the conventional c-GST bonding containing only $Ge\text{-}Te_6$. Conversely, there were few changes in the local structures near the Sb and Te atoms during phase transition, resulting in insignificant peak shifts in the Sb and Te $3d_{5/2}$ orbitals (see Supplementary Fig. S5). This could account for the fast transition and stability in iPCM, as well as the minimal volume change. These results indicated that the local atomic arrangement significantly affected the bonding state, i.e., the meta-valent bonding caused by LRS crystal structures (Fig. 4b) was weakened by a Peierls-like distortion in the HRS as the distortion caused by changes in local structure increased the electron localization, as shown in Fig. 4c.

A detailed switching mechanism associated with Ge atom migration and the reconfiguration of vdW gaps in the SL was proposed with calculation data. [41–44] The atomic images obtained from HAADF-STEM were used to identify the LRS as a specific atomic configuration composed of alternating septuple Ge_3Te_4 and quintuple Sb_2Te_3 layers, where each Ge or Sb sublayer was intermixed at the interface between the two layers, as shown in Fig. 3. The mobility of Ge and Sb atoms during the phase change were evaluated by calculating their diffusion coefficients. The temperature-dependent diffusion coefficient $D(T)$ was defined as the product of the pre-factor, representing the attempt frequency, ν, for escaping, and the Boltzmann factor with the energy barrier, E_b, and temperature, T, as described in the Arrhenius equation:

$$D(T) = \nu e^{-\frac{E_b}{k_B T}} \tag{2}$$

where k_B is the Boltzmann constant. The attempt frequency of each type of atom was estimated from its corresponding energy curve calculated near its equilibrium position, as shown in Supplementary Fig. S7a. Conversely, Supplementary Fig. S7b shows that the energy barrier is extracted directly from the minimum energy path between the original cation layer and the nearest neighboring vdW gap, which was calculated by the nudged elastic band method. [45] Combining these two calculations, the diffusion coefficient in Fig. 5e was evaluated. Ge atoms prefer moving to a vacant site in the nearest neighboring cation layer adjacent to the vdW layer, due to its smaller atomic mass and lower activation energy during the diffusion process. The original Ge layer emptied to become an ordered vacancy layer, whereas the vdW gap partially filled with Ge atoms became a new cation layer, forming the nonuple GST structure in the HRS, as indicated by the new induced XRD peaks in Fig. 2d.

Since the distorted structure of the HRS through Ge vacancies induced Ge-Te short bonds (long bonds) to be shortened (relatively longer), the deviation in the chemical ordering increased compared to LRS, as shown in the Ge layers distortion in the HRS in Fig. 5b–c. This distortion caused by Ge layer vacancies appeared because the vdW gap filled with Ge atoms during the phase change from the LRS to HRS.

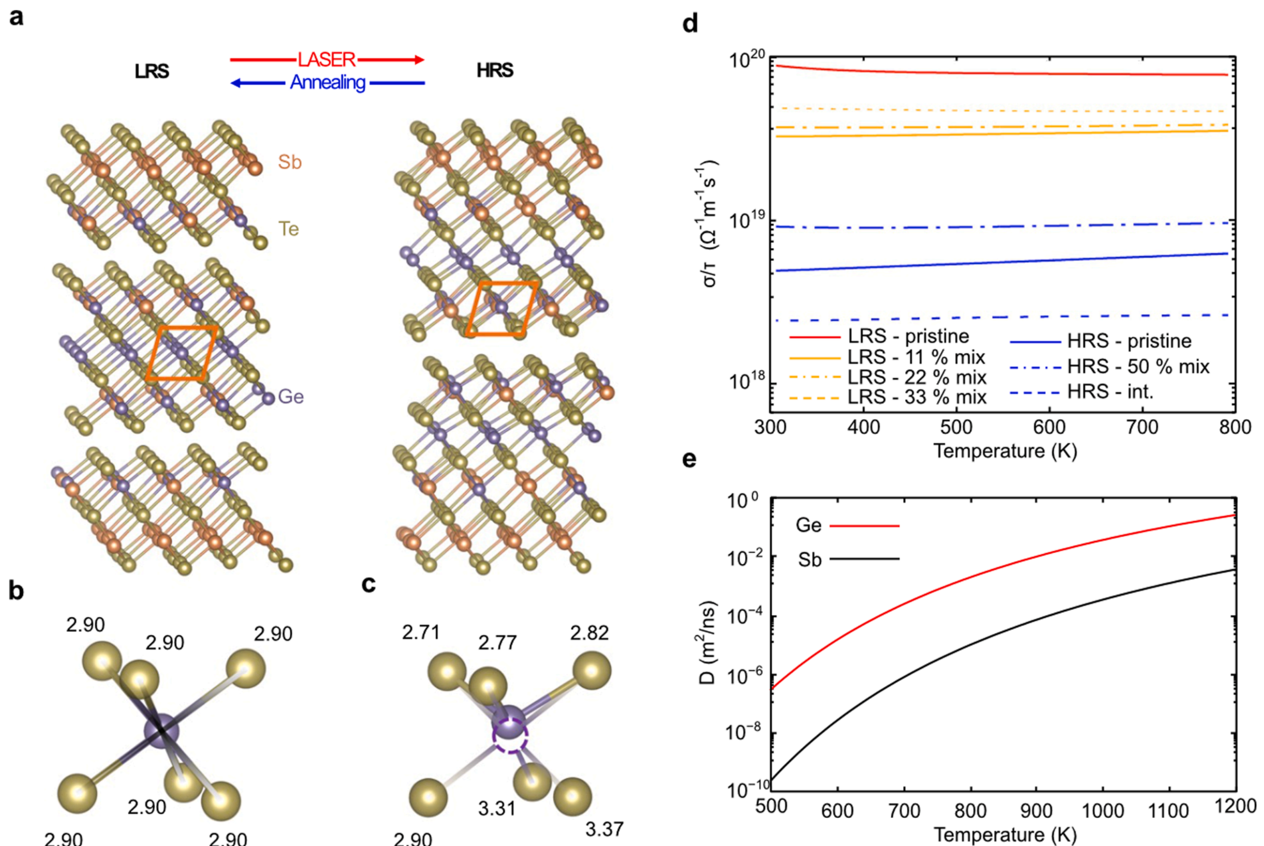

Fig. 5. Computational modeling of the switching process of the Sb_2Te_3/ GeTe SL. a) Schematics of the conceptual mechanism of switching in SL. Ge, Sb, and Te atoms are shown in purple, orange, and dark bronze, respectively. The vdWs layer in the LRS was partially filled with diffused Ge atoms when the phase was changed to the HRS, resulting in the layer containing vacancies in the HRS. The orange boxes indicate locations of Ge-centered octahedral structures. b) Schematic of the octahedral structure with a Ge atom in the center in the LRS and c) in the HRS. The values represent the distance between each Te atom and the central Ge atom in the Angstroms. d) Conductivity per relaxation time of the LRS and HRS with intermixing (mix) or intercalation (int.) along the vertical axis. The effect of intermixing on conductivity was considered in the LRS by changing the intermixing ratios up to 33%. Although the conductivity was affected by the intermixing ratio, the changes were not considerable, i.e., regardless of whether HRS was intermixed or not, the conductivity of LRS was larger than that of HRS. e) Diffusion coefficient of the Ge and Sb atoms during the migration from the cation layer to the vacancy layer.

Consequently, in the LRS structure, the Ge with four valence electrons affected the formation of aligned metavalent bonding, whereas in the HRS structure, the distortion promoted the partial generation of covalent bonding, which was consistent with XPS data changes caused by the structural modulation. Thereafter, the conductivities of the LRS and HRS were calculated using the Boltzmann transport equations with the constant relaxation time approximation to elucidate the difference in resistance due to structural changes. [46] HRS conductivity decreased with vacancy layer intercalations, which was expected as the Te-v-Te distance increased during the phase change in the experiments. A suitable phase-change model through the formation of a defective GST layer is proposed, supported by the confirmation of the structural analysis and chemical bonding properties between the LRS and HRS. Moreover, the change in the charge carrier density, according to the modulation of the orbital configuration caused by the observed Ge atomic structure changes, explained the difference in resistance between the LRS and HRS satisfactorily.

Lower diffusivity and higher activation energy of Sb, compared with those of Ge, as shown in Fig. 5e and S7, respectively, indicate that the migration of the Sb requires more energy than that of Ge. Therefore, reversible phase-change over 10^9 times could be achieved via Ge's transition while suppressing Sb's transition. The atomic movement of heat in the SLs could be classified into two major steps. First, vacancy ordering, as discussed above. Second, the thermal diffusion of GeTe into Sb_2Te_3 QLs, in which the GeTe layers penetrate the middle of the Sb_2Te_3 blocks through thermodynamic tendencies. Since this temperature was relatively high compared to the temperature required for vacancy ordering, trigonal GST blocks (the seven layers block was dominant) were generated, as schematically illustrated in Fig. 6d. The colored arrows in Fig. 6b–c indicate identical areas in the specimen. Cation reordering occurred due to the heat treatment at 200 °C and the number of metastable GST block atomic layers decreased in accordance with the proposed study model. Thereafter, it was observed by comparing the images of T_2 and T_5 (the positions of vdW gaps in T_2–T_4 remained the same) that the vdW gaps located on the red and green arrows moved to the orange and yellow arrows, respectively. After a brief annealing time at 300 °C, a vdW gap located on the yellow arrow disappeared, as shown at T_6. These changes clearly indicated that the number of block layers increased during the 300 °C annealing period, which could imply the formation of the trigonal-GeSbTe (*t*-GST) blocks by the thermal diffusion. After heat treatment at 300 °C for 6 min, 7-layer blocks, such as trigonal-$GeSb_2Te_4$, were formed dominantly without any other QLs in the specimen, as shown in Fig. 6e. Regarding the LRS structure, the GeTe layer between the Sb_2Te_3 layers is strained to form a superlattice structure. Previous reports showed that when the GeTe strain is controlled in the superlattice structure, the bonding strength of the Ge-Te changes, and the crystallization energy changes accordingly. [47–49] However, in the trigonal GST structure, no structure exists in which the GeTe layer is strained between Sb_2Te_3 layers. The SLs in the structure consisting solely of *t*-GST after heat treatment no longer had fast and low energy switching characteristics because of the *t*-GST stability. These results indicated that the device operation failure was the source of reliability of the iPCM. Therefore, the two major steps of atomic movement through heat in the SLs should be dealt with independently and precisely.

Supplementary Fig. S8 depicts an overall concluding schematic diagram of the GeTe/Sb_2Te_3 SL. A relationship between each energy state and phase transition was clearly suggested. Reversible transitions between the HRS and LRS were possible in the SLs by vacancy ordering. However, once 7- or 9-layer dominant *t*-GST blocks without additional QLs were formed by excessive energy, the fast and low energy switching characteristics of the SL were absent. In this state, fast reversible switching was no longer possible in the SL device. Consequently, the annealing effect in the SLs was thoroughly defined.

3. Conclusions

In this study, a large-scale iPCM phase transition was performed through in-situ laser pulse-induced reversible crystalline-to-crystalline phase transformation. Phase-change in the large area allows study on the chemical states to clarify the inconclusive debates that Ge is responsible for the phase-change and transition in the bond type rather than Sb and Te. The experimental observations of the iPCM crystal structure transformation using direct atomic imaging and XRD indicated

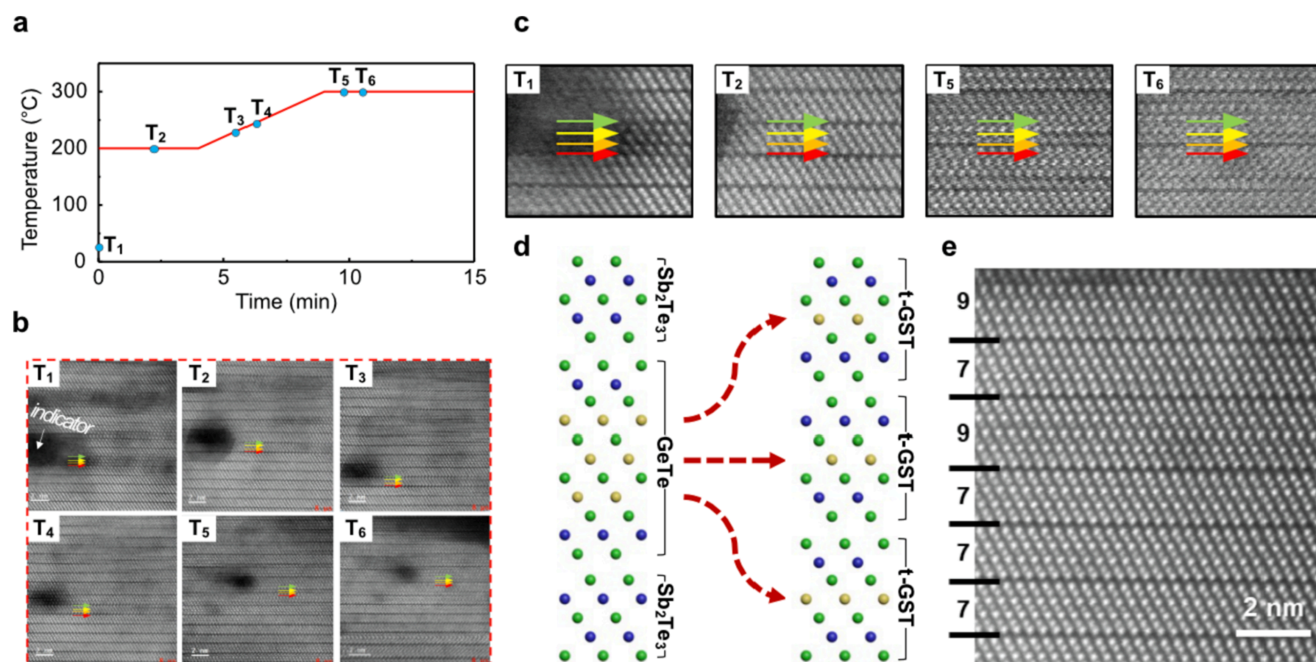

Fig. 6. Atomic-resolution of HAADF-STEM image of vacancy ordering and thermal diffusion of GeTe into Sb_2Te_3 QLs in a Sb_2Te_3/ GeTe SL. a) Diagram showing a plot of annealing time versus annealing temperature. b) and c) Atomic-resolution of HAADF-STEM images of annealing time effects on vdW gaps. The colored arrows indicate identical areas in the specimen. d) Schematics of the thermal diffusion process. e) Formation of GeSbTe blocks without Sb_2Te_3 QLs.

that a GST with a metastable fcc crystal structure was induced in the HRS. The detailed TEM analysis showed the intermixed structure in the LRS and the deformation structure of the c-GST block in the HRS. Moreover, the crystalline phase-changes in long-range orders were clearly observed in the XRD, thus supporting the generation of a metastable fcc GST structure. The chemical state changes of the LRS and HRS using XPS showed the $Ge2p_{3/2}$ binding energy modulation, which could be the reason for the reversible transition by weakening the metavalent bonding. The LRS and HRS, as set and reset states, could explain the difference in conductivity via distortion of Ge local structures and the reconfiguration of vdW gaps, as shown in the crystalline SL structure modeling. These results represent significant progress in the understanding of the phase-change of $GeTe/Sb_2Te_3$ SLs and revealed new possibilities for the industrial development of $GeTe/Sb_2Te_3$ SL-based memory devices based on perceptive engineering of the energy barrier for switching using the local Ge atom structure. Additionally, based on the direct observation in the structural evolutions, we suggest the thermodynamic hierarchies in the cubic, hcp, and amorphous phases. We believe that our study provides comprehensive perspectives to design entropy suppressed system, which is expected to be implemented into various functional materials.

4. Methods

Acetone, methanol, and deionized water were used to remove organic and inorganic substances; thereafter, a BOE solution was employed to remove surface oxidation as a pre-growth treatment. Single-crystal-like quality SL films [GeTe 1 nm/Sb_2Te_3 1 nm]$_5$ / [Sb_2Te_3 10 nm] were grown on *n*-type Si (111) by using MBE and a co-deposition process, which was effective in synthesizing high-quality crystal structures [GeTe 1 nm/Sb_2Te_3 1 nm]$_5$. The Ge, Sb, and Te were evaporated by a Knudsen cell. Each step of the evaporation process was controlled by an individually operated shutter, which was linked with a quartz crystal monitor and programmed system. The first growth step for fabricating a Sb_2Te_3 seed layer included the simultaneous thermal evaporation process (1.6 and 3 Å/min for Sb and Te, respectively, on Si (111) substrates) which was followed a vacuum of 1×10^{-8} Torr at 300 K. [50] Thereafter, a post-annealing process was conducted at 180 °C for 30 min to enhance the Sb_2Te_3 crystallinity. During the annealing process, excess nonstoichiometric Te was diffused out. The second process for fabricating GeTe and Sb_2Te_3 stack structures included the simultaneous thermal evaporation process for Ge-Te and Sb-Te, followed by an in-situ annealing process at 160 °C using a halogen lamp under a vacuum of 1×10^{-8} Torr (1.0, 1.6, and 3.0 Å/min for Ge, Sb and Te, respectively).

To investigate the structural characteristics, XRD measurements were obtained using a conventional high-resolution-XRD system with a Cu Kα beam source. The KrF optical laser, which is a LAMBDA PHYSIK's COMPEX 205 model, has a beam spot size of 200 mm × 200 mm. It is suitable for the phase change observed in XRD. Raman spectra of the $GeSb_2Te_4$ were obtained through micro-Raman spectroscopy (Horiba Lab Ram ARAMIS) using a 532 nm wavelength Nd:YAG laser with a 100 × objective and 2400 grooves/mm grating. The spectra were calibrated at a silicon peak of 520 cm^{-1}. The local atomic structure was analyzed using a high-resolution XPS (PHI 5000 Versaprobe using a monochromatic Al Kα source 1486.6 eV). In-situ transfer vessels were used to avoid surface oxidation of the films. All spectra were calibrated using a carbon reference peak of 284.8 eV.

The cross-sectional specimens for TEM characterization were prepared using a focused ion beam (FIB, NX2000; Hitachi Inc., Japan) instrument. The TEM samples were etched using a Ga^+ ion beam from 30 to 5 keV during the FIB milling process. Thereafter a low-energy Ar^+ ion beam of 1 keV was used for the final milling, to minimize surface damage. A Protochips Fusion holder was used for the in-situ heating experiment. A suitable micro-electromechanical-system-based thermal chip for the holder was used. However, due to the chip structure, attaching the thermal chip directly to the chip by focused ion beam (FIB) work proved challenging. Additionally, when EBID or IBID were used to attach a specimen, deposition material entered the area requiring electron transparent and the target area, which was problematic. Therefore, a method was adopted which transferred the FIB specimen using the electrostatic force of the glass tip.

To investigate the atomic configuration of the LRS and HRS, first-principles calculations based on DFT were performed. Two different cells were adopted, one containing a Ge_3Te_4 block sandwiched between two Sb_2Te_3 blocks for the LRS and the other containing two intermixed $Ge_{1.5}Sb_2Te_5$ blocks. The in-plane lattice constant of the unit cell was 4.25 Å for both structures, similar to that of Sb_2Te_3. The out-of-plane lattice constant was 34.37 and 35.06 Å for the LRS and HRS, respectively. To investigate the intermixed or partially vacant layers, the cells were enlarged to $2 \times 2 \times 1$ and $3 \times 3 \times 1$, containing 68 and 153 atoms, respectively, for the LRS and HRS. All DFT calculations are performed in the Vienna ab initio simulation package [51,52] with a Perdew–Burke–Ernzerhof functional plane-wave basis [51] and projector augmented potentials, [53,54] to investigate the material properties. An energy cutoff of 500 eV was employed in all calculations, and a $2 \times 2 \times 1$ k-grid was employed to sample the Brillouin-zone for the electronic and ionic relaxation due to the large size of the cells. To capture the resistance variation of the phase change, the semi-classic Boltzmann transport equation was solved with the constant relaxation time approximation using the BoltzTraP code. [46] As denser k-girds are required for sampling, they were set at $10 \times 10 \times 4$.

Declaration of Competing Interest

The authors declare that they have no known competing financial interests or personal relationships that could have appeared to influence the work reported in this paper.

Acknowledgments

This research was supported by grants from the Nano Material Technology Development Program through the National Research Foundation of Korea (NRF), funded by the Ministry of Science, ICT, and Future Planning (NRF2016M3A7B4910398); the Ministry of Trade, Industry & Energy (MOTIE) in Korea (Project No. 10080625); the Government of Korea (MSIP) (No. 2021M3H4A1A03052566); the Korea Semiconductor Research Consortium (KSRC); and the National Research Foundation of Korea (NRF) grant funded by the Korea government (MSIP) (No. 2020M3F3A2A0108232413) through a project developing source technologies for future semiconductor devices. We would like to thank Editage (www.editage.co.kr) for English language editing.

Appendix A. Supplementary data

Supplementary data to this article can be found online at https://doi.org/10.1016/j.apsusc.2022.154274.

References

[1] X. Yu, J. Robertson, Modeling of switching mechanism in GeSbTe chalcogenide superlattices, Sci. Rep. 5 (1) (Oct. 2015) 12612, https://doi.org/10.1038/srep12612.

[2] S.R. Ovshinsky, Reversible Electrical Switching Phenomena in Disordered Structures, Phys. Rev. Lett. 21 (20) (Nov. 1968) 1450–1453, https://doi.org/10.1103/PhysRevLett.21.1450.

[3] M.H.R. Lankhorst, B.W.S.M.M. Ketelaars, R.A.M. Wolters, Low-cost and nanoscale non-volatile memory concept for future silicon chips, Nat. Mater. 4 (4) (Apr. 2005) 347–352, https://doi.org/10.1038/nmat1350.

[4] A. Sebastian, M. Le Gallo, R. Khaddam-Aljameh, E. Eleftheriou, Memory devices and applications for in-memory computing, Nat. Nanotechnol. 15 (7) (Jul. 2020) 529–544, https://doi.org/10.1038/s41565-020-0655-z.

[5] J. Shen, S. Jia, N. Shi, Q. Ge, T. Gotoh, S. Lv, Q.i. Liu, R. Dronskowski, S.R. Elliott, Z. Song, M. Zhu, Elemental electrical switch enabling phase segregation–free operation, Science 374 (6573) (2021) 1390–1394.

[6] M. Xu, X. Mai, J. Lin, W. Zhang, Y.i. Li, Y. He, H. Tong, X. Hou, P. Zhou, X. Miao, Recent Advances on Neuromorphic Devices Based on Chalcogenide Phase-Change Materials, Adv. Funct. Mater. 30 (50) (2020) 2003419.
[7] W. Zhang, E. Ma, Unveiling the structural origin to control resistance drift in phase-change memory materials, Mater. Today 41 (Dec. 2020) 156–176, https://doi.org/10.1016/j.mattod.2020.07.016.
[8] B. Liu, K. Li, W. Liu, J. Zhou, L. Wu, Z. Song, S.R. Elliott, Z. Sun, Multi-level phase-change memory with ultralow power consumption and resistance drift, Sci. Bull. 66 (21) (2021) 2217–2224.
[9] P. Ma, H. Tong, M. Xu, X. Cheng, X. Miao, Suppressed resistance drift from short range order of amorphous GeTe ultrathin films, Appl. Phys. Lett. 117 (2) (Jul. 2020), 022109, https://doi.org/10.1063/5.0009362.
[10] K.L. Okabe, A. Sood, E. Yalon, C.M. Neumann, M. Asheghi, E. Pop, K.E. Goodson, H.-S. Wong, Understanding the switching mechanism of interfacial phase change memory, J. Appl. Phys. 125 (18) (2019) 184501.
[11] J. Momand, R. Wang, J.E. Boschker, M.A. Verheijen, R. Calarco, B.J. Kooi, Interface formation of two- and three-dimensionally bonded materials in the case of GeTe–Sb_2Te_3 superlattices, Nanoscale 7 (45) (2015) 19136–19143, https://doi.org/10.1039/C5NR04530D.
[12] T. Ohyanagi, M. Kitamura, M. Araidai, S. Kato, N. Takaura, K. Shiraishi, GeTe sequences in superlattice phase change memories and their electrical characteristics, Appl. Phys. Lett. 104 (25) (Jun. 2014), 252106, https://doi.org/10.1063/1.4886119.
[13] J. Tominaga, A.V. Kolobov, P. Fons, T. Nakano, S. Murakami, Ferroelectric Order Control of the Dirac-Semimetal Phase in GeTe-Sb_2Te_3 Superlattices, Adv. Mater. Interfaces 1 (1) (Feb. 2014) 1300027, https://doi.org/10.1002/admi.201300027.
[14] A.V. Kolobov, P. Fons, Y. Saito, J. Tominaga, Atomic Reconfiguration of van der Waals Gaps as the Key to Switching in GeTe/Sb_2Te_3 Superlattices, ACS Omega 2 (9) (Sep. 2017) 6223–6232, https://doi.org/10.1021/acsomega.7b00812.
[15] R.E. Simpson, P. Fons, A.V. Kolobov, T. Fukaya, M. Krbal, T. Yagi, J. Tominaga, Interfacial phase-change memory, Nat. Nanotechnol. 6 (8) (2011) 501–505.
[16] N.-K. Chen, X.-B. Li, X.-P. Wang, S.-Y. Xie, W.Q. Tian, S. Zhang, H.-B. Sun, Metal–Insulator Transition of Ge–Sb–Te Superlattice: An Electron Counting Model Study, IEEE Trans. Nanotechnol. 17 (1) (2018) 140–146.
[17] B. Casarin, A. Caretta, J. Momand, B.J. Kooi, M.A. Verheijen, V. Bragaglia, R. Calarco, M. Chukalina, X. Yu, J. Robertson, F.R.L. Lange, M. Wuttig, A. Redaelli, E. Varesi, F. Parmigiani, M. Malvestuto, Revisiting the Local Structure in Ge-Sb-Te based Chalcogenide Superlattices, Sci. Rep. 6 (1) (2016), https://doi.org/10.1038/srep22353.
[18] A. Lotnyk, I. Hilmi, U. Ross, B. Rauschenbach, Van der Waals interfacial bonding and intermixing in GeTe-Sb2Te3-based superlattices, Nano Res. 11 (3) (Mar. 2018) 1676–1686, https://doi.org/10.1007/s12274-017-1785-y.
[19] P. Kowalczyk, F. Hippert, N. Bernier, C. Mocuta, C. Sabbione, W. Batista-Pessoa, P. Noé, Impact of Stoichiometry on the Structure of van der Waals Layered GeTe/Sb_2Te_3 Superlattices Used in Interfacial Phase-Change Memory (iPCM) Devices, Small 14 (24) (2018) 1704514.
[20] A. Lotnyk, T. Dankwort, I. Hilmi, L. Kienle, B. Rauschenbach, In situ observations of the reversible vacancy ordering process in van der Waals-bonded Ge–Sb–Te thin films and GeTe–Sb_2Te_3 superlattices, Nanoscale 11 (22) (2019) 10838–10845, https://doi.org/10.1039/C9NR02112D.
[21] J. Momand, R. Wang, J.E. Boschker, M.A. Verheijen, R. Calarco, B.J. Kooi, Dynamic reconfiguration of van der Waals gaps within GeTe–Sb_2Te_3 based superlattices, Nanoscale 9 (25) (2017) 8774–8780, https://doi.org/10.1039/C7NR01684K.
[22] Y. Xu, X. Wang, W. Zhang, L. Schäfer, J. Reindl, F. vom Bruch, Y. Zhou, V. Evang, J.-J. Wang, V.L. Deringer, E.n. Ma, M. Wuttig, R. Mazzarello, Materials Screening for Disorder-Controlled Chalcogenide Crystals for Phase-Change Memory Applications, Adv. Mater. 33 (9) (2021) 2006221.
[23] K. Li, L. Peng, L. Zhu, J. Zhou, Z. Sun, Vacancy-mediated electronic localization and phase transition in cubic Sb2Te3, Mater. Sci. Semicond. Process. 135 (Nov. 2021), 106052, https://doi.org/10.1016/j.mssp.2021.106052.
[24] T.-T. Jiang, X.-D. Wang, J.-J. Wang, Y.-X. Zhou, D.-L. Zhang, L.u. Lu, C.-L. Jia, M. Wuttig, R. Mazzarello, W. Zhang, In situ study of vacancy disordering in crystalline phase-change materials under electron beam irradiation, Acta Mater. 187 (2020) 103–111.
[25] T. Siegrist, P. Jost, H. Volker, M. Woda, P. Merkelbach, C. Schlockermann, M. Wuttig, Disorder-induced localization in crystalline phase-change materials, Nat. Mater. 10 (3) (2011) 202–208.
[26] W. Zhang, A. Thiess, P. Zalden, R. Zeller, P.H. Dederichs, J.-Y. Raty, M. Wuttig, S. Blügel, R. Mazzarello, Role of vacancies in metal–insulator transitions of crystalline phase-change materials, Nat. Mater. 11 (11) (2012) 952–956.
[27] V. Bragaglia, F. Arciprete, W. Zhang, A.M. Mio, E. Zallo, K. Perumal, A. Giussani, S. Cecchi, J.E. Boschker, H. Riechert, S. Privitera, E. Rimini, R. Mazzarello, R. Calarco, Metal - Insulator Transition Driven by Vacancy Ordering in GeSbTe Phase Change Materials, Sci. Rep. 6 (1) (2016), https://doi.org/10.1038/srep23843.
[28] X. Yu, J. Robertson, Atomic Layering, Intermixing and Switching Mechanism in Ge-Sb-Te based Chalcogenide Superlattices, Sci. Rep. 6 (1) (Dec. 2016) 37325, https://doi.org/10.1038/srep37325.
[29] J. Gainza, F. Serrano-Sánchez, N.M. Nemes, O.J. Dura, J.L. Martínez, J.A. Alonso, Lower temperature of the structural transition, and thermoelectric properties in Sn-substituted GeTe, Mater. Today Proc. 44 (2021) 3450–3457, https://doi.org/10.1016/j.matpr.2020.03.044.
[30] M. Boniardi, D. Ielmini, Physical origin of the resistance drift exponent in amorphous phase change materials, Appl. Phys. Lett. 98 (24) (Jun. 2011), 243506, https://doi.org/10.1063/1.3599559.
[31] A. Pirovano, A.L. Lacaita, A. Benvenuti, F. Pellizzer, R. Bez, Electronic Switching in Phase-Change Memories, IEEE Trans. Electron Devices 51 (3) (Mar. 2004) 452–459, https://doi.org/10.1109/TED.2003.823243.
[32] M. Behrens, A. Lotnyk, J.W. Gerlach, I. Hilmi, T. Abel, P. Lorenz, B. Rauschenbach, Ultrafast interfacial transformation from 2D- to 3D-bonded structures in layered Ge–Sb–Te thin films and heterostructures, Nanoscale 10 (48) (2018) 22946–22953.
[33] Y. Zheng, Y. Wang, T. Xin, Y. Cheng, R. Huang, P. Liu, M. Luo, Z. Zhang, S. Lv, Z. Song, S. Feng, Direct atomic identification of cation migration induced gradual cubic-to-hexagonal phase transition in Ge2Sb2Te5, Commun. Chem. 2 (1) (2019), https://doi.org/10.1038/s42004-019-0114-7.
[34] J. Momand, F.R.L. Lange, R. Wang, J.E. Boschker, M.A. Verheijen, R. Calarco, M. Wuttig, B.J. Kooi, Atomic stacking and van-der-Waals bonding in GeTe–Sb_2Te_3 superlattices, J. Mater. Res. 31 (20) (2016) 3115–3124.
[35] A. Klein, et al., Changes in Electronic Structure and Chemical Bonding upon Crystallization of the Phase Change Material GeSb 2 Te 4, Phys. Rev. Lett. 100 (1) (Jan. 2008), 016402, https://doi.org/10.1103/PhysRevLett.100.016402.
[36] V.P. Zlomanov, A.K. Tkalich, 'Charge impurity states of In, Ga, Ge in narrow-gap PbTe', Kiev, Ukraine (Nov. 1999) 158–162, https://doi.org/10.1117/12.368348.
[37] L. V. Yashina, S. P. Kobeleva, T. B. Shatalova, V. P. Zlomanov, and V. I. Shtanov, 'XPS study of fresh and oxidized GeTe and žGe,Sn/ Te surface', p. 10, 2001.
[38] A.V. Kolobov, P. Fons, A.I. Frenkel, A.L. Ankudinov, J. Tominaga, T. Uruga, Understanding the phase-change mechanism of rewritable optical media, Nat. Mater. 3 (10) (Oct. 2004) 703–708, https://doi.org/10.1038/nmat1215.
[39] R.B. Shalvoy, G.B. Fisher, P.J. Stiles, Bond ionicity and structural stability of some average-valence-five materials studied by x-ray photoemission, Phys. Rev. B 15 (4) (Feb. 1977) 1680–1697, https://doi.org/10.1103/PhysRevB.15.1680.
[40] Y. Kim, K. Jeong, M.-H. Cho, U. Hwang, H.S. Jeong, K. Kim, Changes in the electronic structures and optical band gap of Ge2Sb2Te5 and N-doped Ge2Sb2Te5 during phase transition, Appl. Phys. Lett. 90 (17) (Apr. 2007), 171920, https://doi.org/10.1063/1.2722203.
[41] G. Han, F. Liu, W. Li, Y. Huang, N. Sun, F. Ye, Local structure and phase change behavior in interfacial intermixing GeTe–Sb_2Te_3 superlattices, J. Phys. Condens. Matter 32 (25) (Jun. 2020), 255401, https://doi.org/10.1088/1361-648X/ab7577.
[42] B. Li, L. Xu, Y. Guo, and H. Li, 'Internal reverse-biased p-n junctions: a possible origin of the high resistance in phase change superlattice', p. 12.
[43] Y. Saito, A.V. Kolobov, P. Fons, K.V. Mitrofanov, K. Makino, J. Tominaga, J. Robertson, Origin of resistivity contrast in interfacial phase-change memory: The crucial role of Ge/Sb intermixing, Appl. Phys. Lett. 114 (13) (2019) 132102.
[44] W. Chen, H. Li, Native filament-to-dielectric interfaces in phase change superlattice memories, Microelectron. Eng. 215 (Jul. 2019), 111007, https://doi.org/10.1016/j.mee.2019.111007.
[45] H. Jonsson, G. Mills, and K. W. Jacobsen, CHAPTER 16 Nudged elastic band method for nudging minimum energy paths of transitions, p. 20.
[46] G.K.H. Madsen, J. Carrete, M.J. Verstraete, BoltzTraP2, a program for interpolating band structures and calculating semi-classical transport coefficients, Comput. Phys. Commun. 231 (Oct. 2018) 140–145, https://doi.org/10.1016/j.cpc.2018.05.010.
[47] J. Kalikka, X. Zhou, E. Dilcher, S. Wall, J. Li, R.E. Simpson, Strain-engineered diffusive atomic switching in two-dimensional crystals, Nat. Commun. 7 (1) (Sep. 2016) 11983, https://doi.org/10.1038/ncomms11983.
[48] X. Zhou, J. Kalikka, X. Ji, L. Wu, Z. Song, R.E. Simpson, Phase-Change Memory Materials by Design: A Strain Engineering Approach, Adv. Mater. 28 (15) (Apr. 2016) 3007–3016, https://doi.org/10.1002/adma.201505865.
[49] Y. Huang, F. Liu, Y. Zhang, W. Li, G. Han, N. Sun, F. Liu, Effects of biaxial strain on interfacial intermixing and local structures in strain engineered GeTe-Sb2Te3 superlattices, Appl. Surf. Sci. 493 (2019) 904–912.
[50] Y. Saito, P. Fons, L. Bolotov, N. Miyata, A.V. Kolobov, J. Tominaga, A two-step process for growth of highly oriented Sb2Te3 using sputtering, AIP Adv. 6 (4) (Apr. 2016), 045220, https://doi.org/10.1063/1.4948536.
[51] G. Kresse, J. Furthmüller, Efficient iterative schemes for *ab initio* total-energy calculations using a plane-wave basis set, Phys. Rev. B 54 (16) (Oct. 1996) 11169–11186, https://doi.org/10.1103/PhysRevB.54.11169.
[52] G. Kresse, J. Hafner, *Ab initio* molecular dynamics for liquid metals, Phys. Rev. B 47 (1) (Jan. 1993) 558–561, https://doi.org/10.1103/PhysRevB.47.558.
[53] P.E. Blöchl, Projector augmented-wave method, Phys. Rev. B 50 (24) (Dec. 1994) 17953–17979, https://doi.org/10.1103/PhysRevB.50.17953.
[54] G. Kresse, D. Joubert, From ultrasoft pseudopotentials to the projector augmented-wave method, Phys. Rev. B 59 (3) (Jan. 1999) 1758–1775, https://doi.org/10.1103/PhysRevB.59.1758.